## PAPER

Check for updates

# Zero-dimensional organic–inorganic hybrid antimony bromide with efficient broadband orange emission and nonlinear optical response†

Zhao Wang,[a] Xiaoxue Xi 🔟 *[a] and Xueli Chen 🔟 *[b]

The development of lead-free hybrid metal halides with multiple optical properties is essential for advancing perovskite-based optical materials, though it remains challenging. Herein, we synthesized a zero-dimensional (0D) hybrid antimony-based halide, $[DMPZ]_2SbBr_6$ $Br\cdot3H_2O$ (DP-SbBr, DMPZ = $N,N'$-Dimethylpiperazine), *via* precise molecular-level design, which exhibits both efficient photoluminescence (PL) and nonlinear optical (NLO) properties. Notably, DP-SbBr crystallizes in the $P2_12_12$ chiral space group, despite lacking chiral units, with isolated $[SbBr_6]^{3-}$ octahedral units separated by organic molecules, forming a typical 0D hybrid structure. This unique structure enables efficient orange light emission with a 28.5% quantum yield. Additionally, DP-SbBr demonstrates a 0.32-fold second-harmonic generation (SHG) signal relative to KDP, showcasing its potential as a NLO material. This work lays the foundation for designing multifunctional hybrid perovskite-based optical materials at the molecular level.

## Introduction

Three-dimensional (3D) halide perovskites, including $CsPbX_3$ (X = Cl, Br, I), have attracted considerable interest for their remarkable optoelectronic characteristics.[1,2] These properties, such as tunable bandgaps, high defect tolerance, and extensive photoluminescence (PL) spectra spanning from visible to near-infrared, make them suitable for diverse applications like light-emitting diodes (LEDs), solar cells, and X-ray detection.[3–7] However, 3D perovskites exhibit limitations due to the large band dispersion in the corner-sharing 3D network, leading to the facile separation of excitons into free charge carriers at room temperature.[8,9] Additionally, the rigidity and simple chemical composition of the 3D cubic network restrict structural modulation at the molecular level, hindering further optimization of their optical properties.[10]

To address these challenges, low-dimensional hybrid halide perovskites have emerged as promising alternatives, becoming a major focus of current research.[11–15] In particular, zero-dimensional (0D) perovskites display enhanced optical properties and higher PL efficiency, owing to their unique quantum confinement effects.[16–18] In contrast to 3D perovskites, 0D hybrid halides retain quantum confinement and significantly enhance optical properties by incorporating wide-bandgap organic cations that fragment the corner-shared $[PbX_3]^-$ network into discrete 0D units.[19,20] The absence of electronic interactions among the spatially isolated lead halide polyhedra in these 0D hybrid halides results in a flat-band configuration, which effectively confines photoinduced exciton recombination to promote strong electron–phonon coupling, resulting in higher PL efficiency.[21,22] Moreover, the PL properties of 0D perovskites are largely independent of crystal morphology and size, offering superior spectral stability compared to 3D perovskites. These materials exhibit broad spectral emission and high PL quantum yield (PLQY), making them ideal candidates for a variety of optoelectronic applications, such as solid-state lighting, X-ray scintillators and thermometers.[23–25]

Despite the outstanding optoelectronic performance of low-dimensional perovskites, the environmental toxicity of lead remains a significant challenge.[26] Lead-free perovskites can effectively mitigate the environmental risks associated with lead, while also expanding their application range and maintaining or enhancing optoelectronic properties.[27–29] As a result, numerous lead-free hybrid halides, including those based on $In^{3+}$, $Sn^{2+}$, $Bi^{3+}$, $Mn^{2+}$, $Zn^{2+}$, $Cd^{2+}$ and $Sb^{3+}$, have been extensively explored as ideal candidates for solid-state light-emitting materials.[30–36] Among these, Sb-based perovskites have garnered attention due to their low toxicity, wide emission spectrum and high PL efficiency. Notably, $Sb^{3+}$ possesses stereochemically active lone pairs of electrons, which not only promotes efficient PL but also imparts additional optical properties to the material, holding great promise for applications requiring efficient emission and enhanced nonlinear

*[a] Equine Science Research and Horse Doping Control Laboratory, Hubei Provincial Engineering Research Center of Racing Horse Detection and Application Transformation, Wuhan Business University, Wuhan 430056, PR China. E-mail: x2300324512@163.com; wangzhao517@stu.hubu.edu.cn*

*[b] Jiangxi Provincial Key Laboratory of Low-Carbon Solid Waste Recycling, School of Geography and Environmental Engineering, Gannan Normal University, Ganzhou 341000, P. R. China. E-mail: xueli089@foxmail.com*

† Electronic supplementary information (ESI) available. See DOI: https://doi.org/10.1039/d5ra02086g
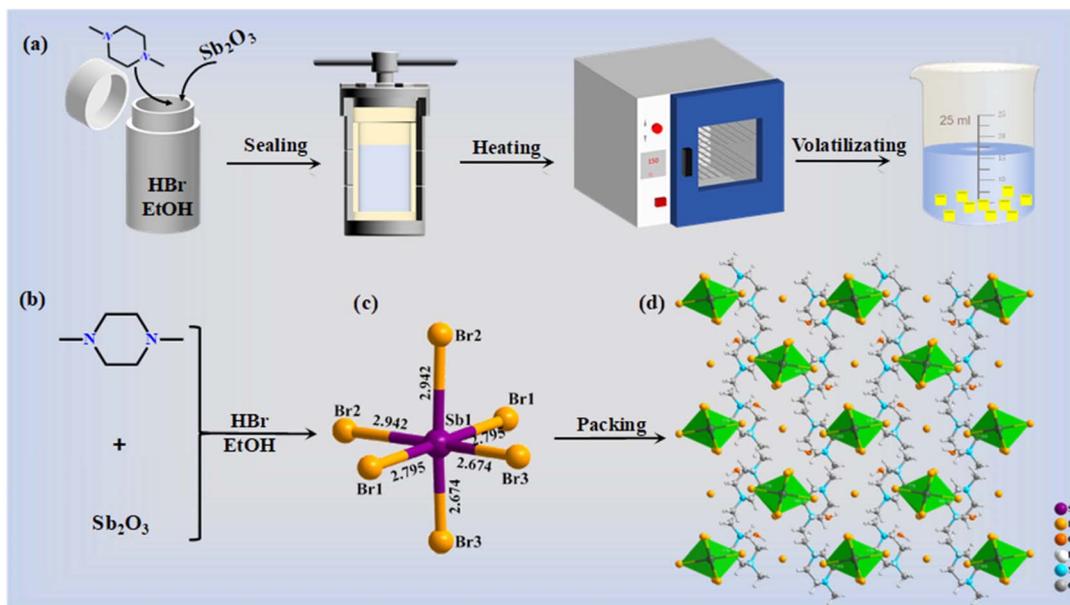
Fig. 1 (a and b) Schematics illustrating the preparation process and structural assembly of DP-SbBr, (c and d) structure packing modes of the DP-SbBr along the $c$-axis.

optical (NLO) behavior.[37,38] In this context, the integration of NLO and PL functionalities within a single material is particularly valuable. Such dual-functional materials not only exhibit efficient light emission, but also respond to high-intensity light through phenomena such as frequency doubling and optical switching. This combination is crucial for the development of compact and multifunctional photonic devices, including tunable light sources, miniaturized lasers, and integrated optical chips. Therefore, the exploration of 0D Sb-based halide perovskites offer significant potential for the development of advanced multifunctional optical materials.

In addition, organic ligands play a pivotal role in modulating the structural and optical properties of hybrid halides. As structure-directing agents, they facilitate the isolation of metal halide units, induce quantum confinement, and stabilize low-dimensional structures, thereby enhancing the material's overall PL performance. Notably, piperazine derivatives, such as $N,N'$-dimethylpiperazine (DMPZ), offer distinct advantages due to their ability to carry a dual charge. This characteristic not only aids in the segregation of metal halide units, leading to the formation of isolated halide species, but also facilitates the incorporation of additional halide ions into lattice. The combination of small, flexible organic ligands with isolated halide units and additional halide ions can induce spatial asymmetry, resulting in distortions within the octahedral structure. Such asymmetry, along with enhanced structural distortions, not only promotes stronger electron–phonon coupling but also amplifies the dipole moment of the structure, which in turn boosts PL efficiency and NLO behavior. Consequently, piperazine-based cations are crucial for tuning the photonic and NLO responses in Sb-based hybrid halides.

Based on the considerations above, we selected DMPZ as the organic template and structure-directing agent to successfully construct a 0D hybrid antimony bromide of $[DMPZ]_2SbBr_6$ $Br \cdot 3H_2O$, abbreviated as DP-SbBr. Notably, DP-SbBr crystallizes in the chiral $P2_12_12$ space group, featuring isolated $[SbBr_6]^{3-}$ octahedral units that are effectively separated by organic molecules, exhibiting significant quantum confinement effects. Thanks to the structural distortion and quantum confinement, the material efficiently promotes the formation of self-trapped excitons (STEs), leading to efficient orange light emission with PLQY of 28.5%. Additionally, the DP-SbBr also exhibits obvious NLO responses, with a second-harmonic generation (SHG) signal that is 0.32 times that of commercial KDP, indicating its potential as a NLO material. Detailed experimental and theoretical studies were conducted to explore its PL mechanism, revealing the profound impact of the structure on optical performance. This work provides a typical example for the design of multifunctional hybrid perovskite materials integrating efficient PL and NLO activity, laying the foundation for advancing the design and development of novel hybrid Sb-based multifunctional optical materials (Fig. 1).

## Results and discussion

The yellow block-like crystals DP-SbBr were prepared via a solvothermal method in a mixed solution of ethanol and hydrobromic acid, with DMPZ as the organic amine and $Sb_2O_3$ as the metal source. X-ray single-crystal diffraction analysis revealed that DP-SbBr crystallized in the orthorhombic $P2_12_12$ space group, featuring 0D $[SbBr_6]^{3-}$ halide anions, one charge-balanced $Br^-$, and three guest $H_2O$ molecules, with protonated DMPZ acting as counter cations and template molecules, facilitating structural regulation of the halide units. Specifically, the $Sb^{3+}$ ion is coordinated with six $Br^-$ ions to form a distorted octahedral structure of $[SbBr_6]^{3-}$, with Sb–Br bond lengths

ranging from 2.674 to 2.972 Å, consistent with the reported values for 0D antimony bromides.[39] The isolated $[SbBr_6]^{3-}$ octahedra are arranged in layers, separated by insulating organic walls, forming a typical 0D structural model. Due to the filling of counterions and guest molecules, the adjacent 0D $[SbBr_6]^{3-}$ units are isolated, with the closest distance being 9.09 Å, indicating weak electronic interaction between the anionic species.[40] The electronic shielding and isolation effect of the organic component on the inorganic units prevent the formation of electronic bands between the halide units, thereby enhancing the quantum confinement effect and making it an ideal low-dimensional halide PL material. Importantly, although the molecular building blocks are themselves achiral, the compound crystallizes in a chiral space group. This emergent chirality is attributed to the directional hydrogen-bonding network formed between the protonated DMPZ cations, isolated $H_2O$ molecules, and charge-balanced $Br^-$ anions (Fig. S1†). These asymmetric supramolecular interactions not only break local inversion symmetry but also induce distortion of the $[SbBr_6]^{3-}$ octahedra, collectively driving the formation of an overall chiral and noncentrosymmetric crystal packing, which represents a powerful approach to constructing noncentrosymmetric materials from achiral precursors.

In general, the PL properties of halides are strongly influenced by their structural distortion. A higher degree of distortion, such as that observed in the $[SbBr_6]^{3-}$ octahedron, plays a critical role in enhancing emission properties, particularly by promoting the formation of self-trapped excitons (STE). To gain a deeper understanding of this relationship, we quantitatively assessed the distortion levels in the $[SbBr_6]^{3-}$ octahedral units by analyzing variations in the Sb–Br bond lengths and Br–Sb–Br bond angles within the octahedral structure, using the following formula:

$$\Delta d = \frac{1}{6}\sum_{n=1}^{6}\left[\frac{d_n - d}{d}\right]^2 \qquad \sigma^2 = \frac{1}{11}\sum_{n=1}^{11}(\theta_n - 90)^2 \qquad (1)$$

where $d_n$ represents the length of a single Sb–Br bond, $d$ is the average bond length, and $\theta_n$ is the bond angle for each Br–Sb–Br unit. The results revealed that the average $\Delta d$ value for $[SbBr_6]^{3-}$ octahedra is $1.52 \times 10^{-3}$ with $\sigma^2$ being 19.76, indicating

a substantial degree of distortion. This increased distortion leads to a more localized electronic environment, which is crucial for the efficient emission of STEs, thereby enhancing PL efficiency.[41,42] Additionally, the structural distortion significantly influences the material's NLO properties. As the distortion degree increases, the dipole moment of the $[SbBr_6]^{3-}$ octahedron becomes more pronounced, that enhanced dipole moment improves the material's interaction with external electromagnetic fields, resulting in a stronger NLO response. The purity of the DP-SbBr crystal was confirmed through powder X-ray diffraction (PXRD) patterns, which closely aligned with the theoretical values (Fig. S2†). Thermogravimetric analysis (TGA) showed a 5.5% weight loss at 155 °C, attributed to the release of three free water molecules (Fig. S3†). Upon removal of the host molecules, the compound retained stability up to 270 °C, demonstrating its excellent thermal stability.

Given that the space group of DP-SbBr belongs to a chiral space group, we employed the Kurtz–Perry powder method to evaluate its NLO behavior.[43] As shown in Fig. 2a, DP-SbBr exhibits a distinct NLO response under 1064 nm laser irradiation, with an intensity approximately 0.32 times that of commercial KDP. The SHG response of the compound is comparable to those of organic–inorganic hybrid halides, such as $(L-Hhis)_2Sb_2Cl_8$ (0.1 × KDP), $(L-Hpro)_2Cd_5Cl_{12}$ (0.2 × KDP), $(C_6H_{14}N)_2SbCl_5$ (0.3 × KDP), $(C_4H_{10}NO)_2SbCl_5$ (0.12 × KDP), $(R$-3-aminopiperidine)SbBr$_5$ (0.6 × KDP) (Table S3†). Furthermore, the NLO response of DP-SbBr with different particle sizes was tested, and the results showed that the SHG intensity increased with particle size in the range of 50–300 μm, indicating its type I phase matching behavior. In addition, theoretical calculations show that the birefringence ($\Delta n$) is calculated as 0.04 at 1064 nm for compound DP-SbBr, which is large enough for phase-matching in the SHG process (Fig. S4†). The above results show that DP-SbBr has the potential to become a NLO crystal material.

The photophysical properties of DP-SbBr were systematically investigated using ultraviolet-visible (UV-vis) absorption spectroscopy, steady-state PL spectroscopy, and time-resolved PL spectroscopy. The UV-vis absorption spectrum reveals that DP-SbBr exhibits broad absorption from 200 to 500 nm, with a cutoff wavelength at 450 nm (Fig. 5a). Using the Tauc formula,
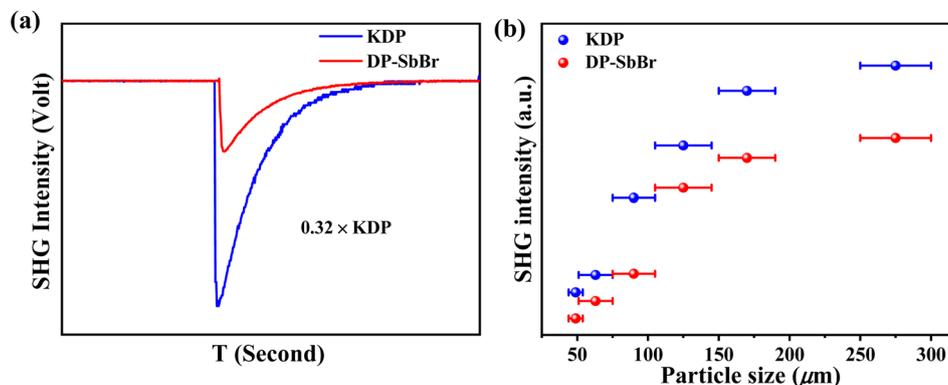


**Fig. 2** (a) The oscilloscope trace of the SHG signals of DP–SbBr and KDP at 1064 nm, (b) size-dependent SHG intensities of DP–SbBr and KDP at 1064 nm.
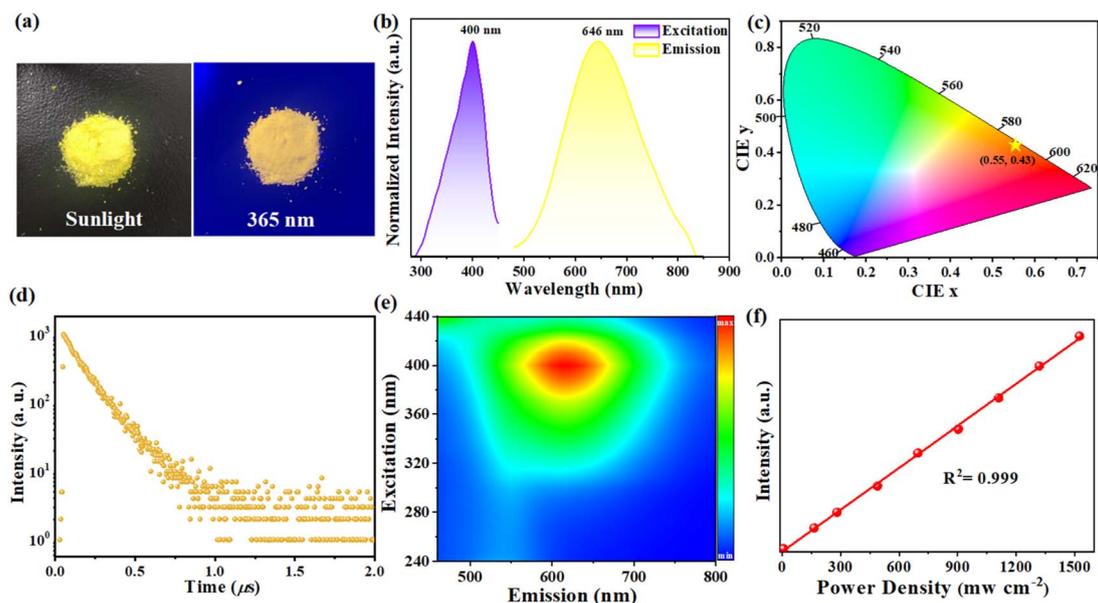
**Fig. 3** The photophysical characterizations of DP–SbBr. (a) Photographs of the crystals under both sunlight and UV lamp irradiation, (b) excitation and emission spectra measured at room temperature, (c) CIE chromaticity coordinates, (d) PL decay curves at room temperature, (e) 3D PL emission spectra as a function of excitation wavelength, and (f) excitation power dependence of the PL intensity.

$$\alpha h\nu = A\left(h\nu - E_\mathrm{g}\right)^{\frac{n}{2}}$$

where $A$ is the proportionality constant, $E_\mathrm{g}$ is the band gap, $h$ is Planck's constant, $\alpha$ is the absorption coefficient, and $\nu$ is the optical frequency and the optical band gap was calculated to be 2.82 eV, corresponding to the color of the crystal, and indicating its broadband semiconductor property (Fig. S5†). As shown in Fig. 3a, the crystal of DP–SbBr emits a bright orange light under 365 nm ultraviolet illumination. The PL excitation spectrum shows a peak excitation wavelength of 400 nm, closely corresponding to the strongest absorption peak. Upon excitation with UV light at 400 nm, DP–SbBr displays a broad Gaussian-shaped emission spectrum, peaking at 646 nm with a full width at half maximum (FWHM) of 175 nm and a Stokes shift of 246 nm (Fig. 3b). The calculated Commission Internationale de l'Éclairage (CIE) chromaticity coordinates are (0.55, 0.43), indicating orange light emission (Fig. 3c). Importantly, the peak emission wavelength, FWHM, and Stokes shift of DP–SbBr are notably larger compared to most previously reported 0D antimony halides, highlighting the significant role of the highly distorted 0D structure in determining the PL properties of the metal halide units. More importantly, due to the strong distortion and twisting within the octahedral environment, DP–SbBr achieves a high PLQY of 28.5% at room temperature (Fig. S6†). This remarkable broadband emission efficiency not only originates from the strong quantum confinement effect of the organic matrix but is also closely related to its own substantial distortion.[37] While the PLQY is lower than the highest reported values, it remains competitive among lead-free materials with integrated NLO activity, which may be related to non-radiative decay promoted by dynamic hydrogen bonding between isolated water molecules and flexible organic cations.

To further reveal the photophysical process of broadband orange emission, time-resolved PL spectroscopy was conducted at room temperature to monitor the peak emission wavelength. As illustrated in Fig. 3d, the PL decay curve was fitted to a single exponential function, yielding a lifetime of 0.14 μs, which is comparable to that of reported 0D antimony halides.[44] To investigate the intrinsic properties of the orange emission of DP–SbBr, the excitation wavelength-dependent 3D emission spectrum was recorded over the range of 240 to 440 nm. As depicted in Fig. 3e, a single emission center was observed across the entire excitation range, with no noticeable shift in peak position or change in shape. This indicates that the broadband light emission arises from the radiative relaxation of a single excited state. Additionally, the relationship between the PL intensity and excitation power was examined at room temperature, revealing a linear dependence, which further supports the idea that the broadband emission of DP–SbBr is intrinsic to its properties, rather than being due to surface defects (Fig. 3f).[45] In conclusion, the broadband PL of DP–SbBr is attributed to the radiative recombination of STEs, as evidenced by the large emission wavelength, considerable structural distortion, wide FWHM and substantial Stokes shift.[46]

To further investigate the underlying mechanism of broadband emission, temperature-dependent emission spectroscopy was conducted in the range of 300 to 80 K. As shown in Fig. 4a, with decreasing temperature, only a single emission peak of broadband orange light was observed without emission splitting, indicating that the broadband orange emission of DP–SbBr is not attributable to multiple radiative mechanisms. However, the maximum emission wavelength experiences a slight redshift, shifting from 646 to 680 nm during the cooling process. Typically, such a shift in the emission peak with
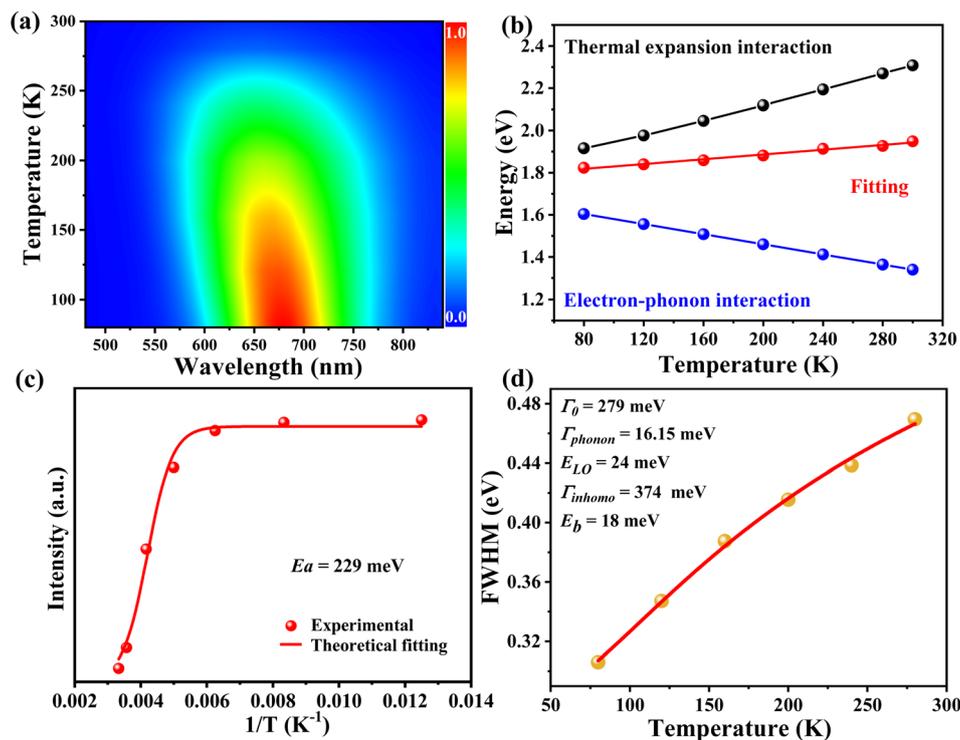
Fig. 4 The temperature-dependent PL characteristics of DP-SbBr. (a) 3D emission spectra as a function of temperature, (b) temperature-dependent evolution of emission energy, highlighting the contributions of thermally activated emission (TE) and exciton–phonon (EP) interactions, (c) integrated PL intensity plotted against the reciprocal temperature, and (d) temperature dependence of the FWHM, accompanied by theoretical fitting for DP-SbBr.

temperature is ascribed to the combined effects of thermal expansion (TE) and electron–phonon (EP) interactions.[47] To model the temperature dependence of the emission energy, $E_g(T)$, a single-oscillator model is used, assuming a linear relationship between thermal expansion and temperature. The evolution of the emission energy with temperature can then be fitted using the following equation:

$$E_g(T) = E_0 + A_{TE} + A_{EP}\left[\frac{2}{e^{\left(\frac{h\omega}{k_B T}\right)} - 1} + 1\right]$$

where $E_0$ is the unrenormalized band gap, $h\omega$ is the average optical phonon energy, $k_B$ is Boltzmann constant, $A_{TE}$ and $A_{EP}$ are the coefficients representing the contributions of thermal expansion (TE) and electron–phonon (EP) interactions, respectively. The TE interaction weakens with decreasing temperature, resulting in a narrowing of the energy gap between the conduction band and the valence band, which leads to a reduction in the band gap. Consequently, the slight redshift observed in the emission energy is primarily attributed to the TE interaction (Fig. 4b).[48] As the thermally activated nonradiative decay weakens during cooling, the emission intensity gradually increases. The temperature-dependent emission intensity was fitted using an Arrhenius-type model:

$$I_{PL} = \frac{I_0}{1 + Ae^{-\frac{E_a}{k_B T}}}$$

$I_0$ and $I_{PL}$ represent the integrated emission intensities at 0 K and at different temperatures ($T$), respectively, while $E_a$ denotes the activation energy and $k_B$ is the Boltzmann constant. The activation energy $E_a$ is determined to be 229 meV, which is significantly higher than the thermal energy of free excitons at room temperature (26 meV). This suggests that stable STEs can be formed effectively suppressing thermal quenching (Fig. 4c).[49,50] At the same time, due to enhanced electron–phonon coupling, the emission FWHM narrows considerably as the temperature decreases. This temperature-dependent behavior of FWHM can be evaluated by fitting the data using the following model:

$$\Gamma(T) = \Gamma_0 + \Gamma_{phonon}(e^{E_{LO}/k_B T} - 1)^{-1} + \Gamma_{inhomo}e^{-E_b/k_B T}$$

In this model, $\Gamma_0$ represents the FWHM at 0 K, $E_{LO}$ is the energy of longitudinal optical phonons, $E_b$ denotes the average binding energy of trap states, and $\Gamma_{phonon}$ and $\Gamma_{inhomo}$ describe the inhomogeneous broadening caused by electron–phonon coupling and trap states, respectively. As illustrated in Fig. 4d, the best fit indicates that the broadband emission is mainly attributed to electron–phonon coupling, with a $\Gamma_{phonon}$ value of 16.15 meV. Furthermore, the phonon energy $E_{LO}$ is calculated to be 24 meV, which matches the Sb–Br stretching frequency (117 cm$^{-1}$) observed in the raman spectrum, thereby providing additional evidence of strong electron–phonon interaction within the $[SbBr_6]^{3-}$ octahedron (Fig. S7†).[30,51] These findings underscore the enhancement of electron–phonon coupling in
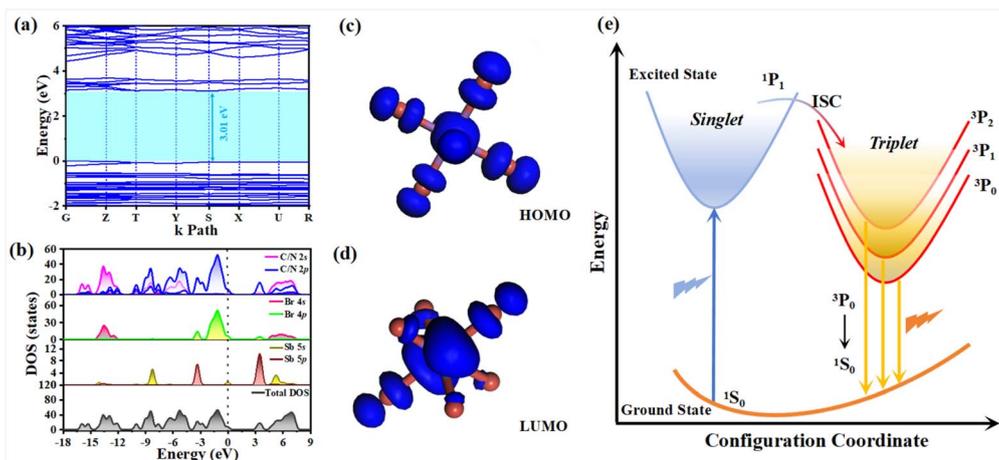
**Fig. 5** (a and b) The calculated band structure and orbital-resolved density of states of DP-SbBr, (c and d) electron maps of HOMO and LUMO, (e) the proposed PL mechanism illustrated in the configuration coordinate diagram of DP-SbBr.

the flexible 0D lattice, further supporting the STE-based nature of the broadband emission.

To further confirm the PL mechanism, we performed first-principles calculations on DP-SbBr to gain deeper insight into its electronic structure and photophysical behavior. As shown in Fig. 5a, the calculated band structure reveals a direct band gap of 3.01 eV, which corresponds well with the optical band gap derived from UV-vis absorption spectroscopy. The total and partial density of states (DOS) analysis indicates that the conduction band minimum (CBM) and valence band maximum (VBM) are predominantly composed of Br-4p, Sb-5p, C-2p, and N-2p orbitals, primarily contributed by the anionic metal halide units and organic cations. Specifically, the VBM is dominated by hybridized Sb-5p and Br-4p states, with minor contributions from the C/N 2p orbitals of the organic moiety, while the CBM is mainly derived from Sb-5p orbitals (Fig. 5b). To better understand the excited-state behavior, we visualized the spatial distribution of the HOMO and LUMO (Fig. 5c and d), both of which are highly localized within the inorganic $[SbBr_6]^{3-}$ units. This suggests that the photoexcited electrons and holes are confined within the same metal halide cluster, favoring localized exciton formation rather than long-range charge separation. Such confinement is consistent with the zero-dimensional structural nature and supports the formation of STEs through strong electron–phonon coupling. The detailed PL mechanism is illustrated in Fig. 5e. Upon UV light excitation, electrons transition quickly from the ground state ($^1S_0$) to the excited state. This photoexcitation is accompanied by structural deformation due to the strong electron–phonon coupling effect, which facilitates the formation of STEs *via* intersystem crossing from the singlet state ($^1P_1$) to the triplet state ($^3P_n$). Ultimately, radiative decay from the lowest $^3P_n$ state to the ground state leads to broadband orange light emission, characterized by a large Stokes shift.[52,53]

Furthermore, we evaluated the structural and optical stability of DP-SbBr under various extreme conditions to assess its suitability for practical applications. The results indicate that

after one week of exposure to a humid environment, both the PXRD patterns and PL emission spectra remain identical to those of the freshly synthesized sample (Fig. S8†). In addition, after 24 hours of continuous exposure to intense ultraviolet light, only a slight reduction in emission intensity was observed, suggesting the material exhibits robust photophysical stability, further corroborated by the PXRD patterns with no significant changes before and after irradiation (Fig. S9†). These findings confirm that DP-SbBr demonstrates excellent structural integrity and luminescent stability, making it highly resilient to varying environmental conditions and suitable for practical applications.

To verify the suitability of the material for solid-state LED devices, we fabricated a white light LED by combining our DP-SbBr sample with commercially available $BaMgAl_{10}O_{17}:Eu^{2+}$
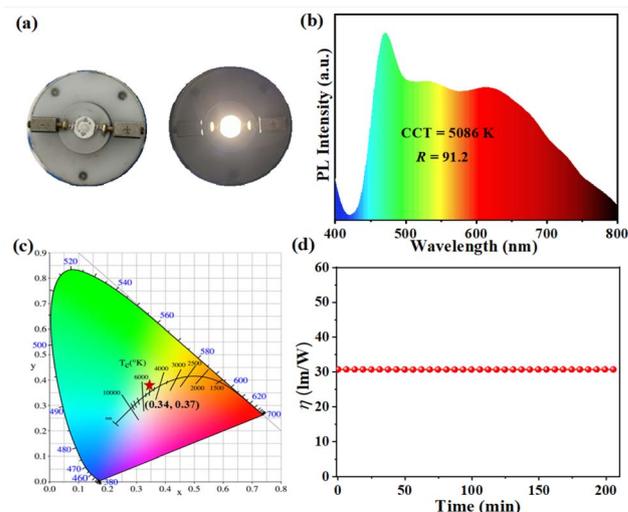


**Fig. 6** Characterizations of white LED fabricated on a UV LED chip: (a) photograph of fabricated WLED, (b) the EL spectra at 20 mA drive current, (c) the CIE chromaticity coordinates, (d) the operating time dependent luminous efficiency.

(blue) and $(Sr,Ba)_2SiO_4$:Eu (green) phosphors. As shown in Fig. 6a, the resulting white light LED emits bright white light at a current of 20 mA. The electroluminescence (EL) emission spectrum of the white light LED spans the entire visible light region, with a correlated color temperature (CCT) of 5086 K and CIE color coordinates of (0.34, 0.37) (Fig. 6b and c). Its color rendering index (CRI) reaches 91.2, significantly higher than the values of conventional fluorescent phosphor materials (approximately 65) and is close to that of natural white light. Moreover, the luminous intensity and efficiency remain stable after continuous operation for 200 minutes, demonstrating the excellent optical stability of the WLED (Fig. 6d).

## Conclusions

In conclusion, we successfully synthesized a 0D hybrid Sb-based halide of DP-SbBr through precise molecular-level design, which exhibits both efficient PL and NLO properties. The unique 0D structure of DP-SbBr, composed of isolated $[SbBr_6]^{3-}$ octahedral units separated by organic molecules, induces quantum confinement effects that efficiently promote STE formation, resulting in a high PLQY and NLO, highlighting its potential as multifunctional optical material. Structural analysis, supported by both experimental and theoretical studies, reveals the crucial role of molecular design in enhancing optical performance. This work presents a novel example of multifunctional hybrid perovskite materials that combine efficient PL and NLO properties, laying the foundation for the development of advanced Sb-based hybrid optical materials for various applications in photonics and optoelectronics.

## Data availability

The data supporting this article are provided as part of the ESI.† Raw experimental data are available from the corresponding author on reasonable request.

## Conflicts of interest

The authors declared that they have no conflicts of interest to this work.

## Acknowledgements

## References

1 L. N. Quan, F. P. García de Arquer, R. P. Sabatini and E. H. Sargent, Perovskites for Light Emission, *Adv. Mater.*, 2018, **30**, 1801996.

2 H. Chen, L. Zhu, C. Xue, P. Liu, X. Du, K. Wen, H. Zhang, L. Xu, C. Xiang, C. Lin, M. Qin, J. Zhang, T. Jiang, C. Yi, L. Cheng, C. Zhang, P. Yang, M. Niu, W. Xu, J. Lai, Y. Cao, J. Chang, H. Tian, Y. Jin, X. Lu, L. Jiang, N. Wang, W. Huang and J. Wang, Efficient and bright warm-white electroluminescence from lead-free metal halides, *Nat. Commun.*, 2021, **12**, 1421.

3 J. Shamsi, A. S. Urban, M. Imran, L. De Trizio and L. Manna, Metal Halide Perovskite Nanocrystals: Synthesis, Post-Synthesis Modifications, and Their Optical Properties, *Chem. Rev.*, 2019, **119**, 3296–3348.

4 S. Li, J. Luo, J. Liu and J. Tang, Self-Trapped Excitons in All-Inorganic Halide Perovskites: Fundamentals, Status, and Potential Applications, *J. Phys. Chem. Lett.*, 2019, **10**, 1999–2007.

5 J. Chen, H. Xiang, J. Wang, R. Wang, Y. Li, Q. Shan, X. Xu, Y. Dong, C. Wei and H. Zeng, Perovskite White Light Emitting Diodes: Progress, Challenges, and Opportunities, *ACS Nano*, 2021, **15**, 17150–17174.

6 Y. He, J. Yan, L. Xu, B. Zhang, Q. Cheng, Y. Cao, J. Zhang, C. Tao, Y. Wei, K. Wen, Z. Kuang, G. M. Chow, Z. Shen, Q. Peng, W. Huang and J. Wang, Perovskite Light-Emitting Diodes with Near Unit Internal Quantum Efficiency at Low Temperatures, *Adv. Mater.*, 2021, **33**, 2006302.

7 Y. Zhou, J. Chen, O. M. Bakr and O. F. Mohammed, Metal Halide Perovskites for X-ray Imaging Scintillators and Detectors, *ACS Energy Lett.*, 2021, **6**, 739–768.

8 H. Lin, C. Zhou, Y. Tian, T. Siegrist and B. Ma, Low-Dimensional Organometal Halide Perovskites, *ACS Energy Lett.*, 2018, **3**, 54–62.

9 Y. Han, S. Yue and B.-B. Cui, Low-Dimensional Metal Halide Perovskite Crystal Materials: Structure Strategies and Luminescence Applications, *Adv. Sci.*, 2021, **8**, 2004805.

10 C. Zhou, L.-J. Xu, S. Lee, H. Lin and B. Ma, Recent Advances in Luminescent Zero-Dimensional Organic Metal Halide Hybrids, *Adv. Opt. Mater.*, 2021, **9**, 2001766.

11 M. I. Saidaminov, O. F. Mohammed and O. M. Bakr, Low-Dimensional-Networked Metal Halide Perovskites: The Next Big Thing, *ACS Energy Lett.*, 2017, **2**, 889–896.

12 A. Singh, B. Yuan, M. H. Rahman, H. Yang, A. De, J. Y. Park, S. Zhang, L. Huang, A. Mannodi-Kanakkithodi, T. J. Pennycook and L. Dou, Two-Dimensional Halide Pb-Perovskite–Double Perovskite Epitaxial Heterostructures, *J. Am. Chem. Soc.*, 2023, **145**, 19885–19893.

13 V. Morad, Y. Shynkarenko, S. Yakunin, A. Brumberg, R. D. Schaller and M. V. Kovalenko, Disphenoidal Zero-Dimensional Lead, Tin, and Germanium Halides: Highly Emissive Singlet and Triplet Self-Trapped Excitons and X-ray Scintillation, *J. Am. Chem. Soc.*, 2019, **141**, 9764–9768.

14 E. Shi, B. Yuan, S. B. Shiring, Y. Gao, Akriti, Y. Guo, C. Su, M. Lai, P. Yang, J. Kong, B. M. Savoie, Y. Yu and L. Dou, Two-dimensional halide perovskite lateral epitaxial heterostructures, *Nature*, 2020, **580**, 614–620.

15 Z. Huang, E. Zhao, P. Qia and A. Song, Zero-dimensional antimony halides with tunable photoluminescence via halogen ligand modulation, *J. Mater. Chem. C*, 2023, **11**, 15742–15749.

16 S. Sun, M. Lu, X. Gao, Z. Shi, X. Bai, W. W. Yu and Y. Zhang, 0D Perovskites: Unique Properties, Synthesis, and Their Applications, *Adv. Sci.*, 2021, **8**, 2102689.

17 J. Zhou, M. Li, L. Ning, R. Zhang, M. S. Molokeev, J. Zhao, S. Yang, K. Han and Z. Xia, Broad-Band Emission in a Zero-Dimensional Hybrid Organic [PbBr$_6$] Trimer with Intrinsic Vacancies, *J. Phys. Chem. Lett.*, 2019, **10**, 1337–1341.

18 H. Chen, B. An, G. Peng, S. Wang, Z. Li, J. Sun, W. Lan, J. Fu, H. Wang, L. Ding and Z. Jin, High-Quality 0D Cs4PbBr6-Based Dense Wafer for High-Sensitivity X-Ray Detection and High-Resolution Imaging in Harsh Environment, *Adv. Opt. Mater.*, 2022, **11**, 2202157.

19 Z. Tang and A. M. Guloy, A Methylviologen Lead(II) Iodide: Novel [PbI$_3^-$]$_\infty$ Chains with Mixed Octahedral and Trigonal Prismatic Coordination, *J. Am. Chem. Soc.*, 1999, **121**, 452–453.

20 J.-Q. Zhao, C.-Q. Jing, J.-H. Wu, W.-F. Zhang, L.-J. Feng, C.-Y. Yue and X.-W. Lei, Systematic Approach of One-Dimensional Lead Perovskites with Face-Sharing Connectivity to Realize Efficient and Tunable Broadband Light Emission, *J. Phys. Chem. C*, 2021, **125**, 10850–10859.

21 Q. A. Akkerman, S. Park, E. Radicchi, F. Nunzi, E. Mosconi, F. De Angelis, R. Brescia, P. Rastogi, M. Prato and L. Manna, Nearly Monodisperse Insulator Cs$_4$PbX$_6$ (X = Cl, Br, I) Nanocrystals, Their Mixed Halide Compositions, and Their Transformation into CsPbX$_3$ Nanocrystals, *Nano Lett.*, 2017, **17**, 1924–1930.

22 Q. Li, Z. Chen, M. Li, B. Xu, J. Han, Z. Luo, L. Tan, Z. Xia and Z. Quan, Pressure-Engineered Photoluminescence Tuning in Zero-Dimensional Lead Bromide Trimer Clusters, *Angew. Chem., Int. Ed.*, 2021, **60**, 2583–2587.

23 Z. Ma, Z. Shi, C. Qin, M. Cui, D. Yang, X. Wang, L. Wang, X. Ji, X. Chen, J. Sun, D. Wu, Y. Zhang, X. J. Li, L. Zhang and C. Shan, Stable Yellow Light-Emitting Devices Based on Ternary Copper Halides with Broadband Emissive Self-Trapped Excitons, *ACS Nano*, 2020, **14**, 4475–4486.

24 N. Lin, X. Wang, H.-Y. Zhang, K.-Q. Sun, L. Xiao, X.-Y. Zhang, C.-Y. Yue, L. Han, Z.-W. Chen and X.-W. Lei, Zero-Dimensional Copper(I) Halide Microcrystals as Highly Efficient Scintillators for Flexible X-ray Imaging, *ACS Appl. Mater. Interfaces*, 2024, **16**, 41165–41175.

25 Q. Hu, C. Zhang, X. Wu, G. Liang, L. Wang, X. Niu, Z. Wang, W.-D. Si, Y. Han, R. Huang, J. Xiao and D. Sun, Highly Effective Hybrid Copper(I) Iodide Cluster Emitter with Negative Thermal Quenched Phosphorescence for X-Ray Imaging, *Angew. Chem., Int. Ed.*, 2023, **62**, e202217784.

26 R. Zhang, H. Xie, Q. Zhao, Z. Tang, C. Yang and B. Su, Zero-Dimensional Hybrid Antimony Chloride with Near-Unity Broad-Band Orange-Red Emission toward Solid-State Lighting, *Inorg. Chem.*, 2023, **62**, 19771–19779.

27 Z. Ma, L. Wang, X. Ji, X. Chen and Z. Shi, Lead-Free Metal Halide Perovskites and Perovskite Derivatives as an Environmentally Friendly Emitter for Light-Emitting Device Applications, *J. Phys. Chem. Lett.*, 2020, **11**, 5517–5530.

28 B. Yang, F. Hong, J. Chen, Y. Tang, L. Yang, Y. Sang, X. Xia, J. Guo, H. He, S. Yang, W. Deng and K. Han, Colloidal Synthesis and Charge-Carrier Dynamics of Cs$_2$AgSb$_{1-y}$Bi$_y$X$_6$ (X: Br, Cl; $0 \leq y \leq 1$) Double Perovskite Nanocrystals, *Angew. Chem., Int. Ed.*, 2019, **58**, 2278–2283.

29 J.-Q. Zhao, Y.-Y. Ma, X.-J. Zhao, Y.-J. Gao, Z.-Y. Xu, P.-C. Xiao, C.-Y. Yue and X.-W. Lei, Stepwise Crystalline Structural Transformation in 0D Hybrid Antimony Halides with Triplet Turn-on and Color-Adjustable Luminescence Switching, *Research*, 2023, **6**, 0094.

30 Y. Liu, Z. Luo, Y. Wei, C. Li, Y. Chen, X. He, X. Chang and Z. Quan, Integrating Achiral and Chiral Organic Ligands in Zero-Dimensional Hybrid Metal Halides to Boost Circularly Polarized Luminescence, *Angew. Chem., Int. Ed.*, 2023, **62**, e202306821.

31 L. Lanzetta, J. M. Marin-Beloqui, I. Sanchez-Molina, D. Ding and S. A. Haque, Two-Dimensional Organic Tin Halide Perovskites with Tunable Visible Emission and Their Use in Light-Emitting Devices, *ACS Energy Lett.*, 2017, **2**, 1662–1668.

32 N. Shen, J. Li, Z. Wu, B. Hu, C. Cheng, Z. Wang, L. Gong and X. Huang, α- and β-[Bmim][BiCl4(2,2′-bpy)]: Two Polymorphic Bismuth-Containing Ionic Liquids with Crystallization-Induced Phosphorescence, *Chem.–Eur. J.*, 2017, **23**, 15795–15804.

33 Y.-Y. Ma, Y.-R. Song, W.-J. Xu, Q.-Q. Zhong, H.-Q. Fu, X.-L. Liu, C.-Y. Yue and X.-W. Lei, Solvent-free mechanochemical syntheses of microscale lead-free hybrid manganese halides as efficient green light phosphors, *J. Mater. Chem. C*, 2021, **9**, 9952–9961.

34 J.-Q. Zhao, D.-Y. Wang, T.-Y. Yan, Y.-F. Wu, Z.-L. Gong, Z.-W. Chen, C.-Y. Yue, D. Yan and X.-W. Lei, Synchronously Improved Multiple Afterglow and Phosphorescence Efficiencies in 0D Hybrid Zinc Halides with Ultrahigh Anti-Water Stabilities, *Angew. Chem., Int. Ed.*, 2024, **63**, e202412350.

35 J.-Q. Zhao, H. Ge, Y.-F. Wu, W.-J. Xu, K. Xu, J.-Q. Ma, Q.-L. Yang, C.-Y. Yue and X.-W. Lei, Crystal rigidifying strategy toward hybrid cadmium halide to achieve highly efficient and narrowband blue light emission, *Mater. Today Chem.*, 2022, **24**, 100766.

36 J.-Q. Zhao, H.-S. Shi, L.-R. Zeng, H. Ge, Y.-H. Hou, X.-M. Wu, C.-Y. Yue and X.-W. Lei, Highly emissive zero-dimensional antimony halide for anti-counterfeiting and confidential information encryption-decryption, *Chem. Eng. J.*, 2022, **431**, 134336.

37 B. Zhou, Y. Muhammad, D. Ding, Z. Liu, H. Hu, Y. Wang, H. Zhong, Y. Shi and H. Li, Dexter Energy Transfer in Zero-Dimensional Inorganic Metal Halides for Obtaining Near-Unity PLQY via Sb$^{3+}$/Mn$^{2+}$ Codoping, *J. Phys. Chem. C*, 2024, **128**, 571–579.

38 Z. Qi, Y. Chen, H. Gao, F.-Q. Zhang, S.-L. Li and X.-M. Zhang, Two SbX$_5$-based isostructural polar 1D hybrid antimony halides with tunable broadband emission, nonlinear optics, and semiconductor properties, *Sci. China Chem.*, 2021, **64**, 2111–2117.

39 F. Lin, H. Wang, W. Liu and J. Li, Zero-dimensional ionic antimony halide inorganic–organic hybrid with strong greenish yellow emission, *J. Mater. Chem. C*, 2020, **8**, 7300–7303.

40 J. Q. Zhao, M. F. Han, X. J. Zhao, Y. Y. Ma, C. Q. Jing, H. M. Pan, D. Y. Li, C. Y. Yue and X. W. Lei, Structural

Dimensionality Modulation toward Enhanced Photoluminescence Efficiencies of Hybrid Lead-Free Antimony Halides, *Adv. Opt. Mater.*, 2021, **9**, 2100556.

41  B. Su, S. Geng, Z. Xiao and Z. Xia, Highly Distorted Antimony (III) Chloride $[Sb_2Cl_8]^{2-}$ Dimers for Near-Infrared Luminescence up to 1070 nm, *Angew. Chem., Int. Ed.*, 2022, **61**, e202208881.

42  Q. Wei, T. Chang, R. Zeng, S. Cao, J. Zhao, X. Han, L. Wang and B. Zou, Self-Trapped Exciton Emission in a Zero-Dimensional $(TMA)_2SbCl_5 \cdot DMF$ Single Crystal and Molecular Dynamics Simulation of Structural Stability, *J. Phys. Chem. Lett.*, 2021, **12**, 7091–7099.

43  J. Wu, Y. Guo, J. L. Qi, W. D. Yao, S. X. Yu, W. Liu and S. P. Guo, Multi-Stimuli Responsive Luminescence and Domino Phase Transition of Hybrid Copper Halides with Nonlinear Optical Switching Behavior, *Angew. Chem., Int. Ed.*, 2023, **62**, e202301937.

44  L. Lian, P. Zhang, X. Zhang, Q. Ye, W. Qi, L. Zhao, J. Gao, D. Zhang and J. Zhang, Realizing Near-Unity Quantum Efficiency of Zero-Dimensional Antimony Halides through Metal Halide Structural Modulation, *ACS Appl. Mater. Interfaces*, 2021, **13**, 58908–58915.

45  Y. Jing, Y. Liu, M. Li and Z. Xia, Photoluminescence of Singlet/Triplet Self-Trapped Excitons in $Sb^{3+}$-Based Metal Halides, *Adv. Opt. Mater.*, 2021, **9**, 2002213.

46  H. Liu, T. B. Shonde, F. Gonzalez, O. J. Olasupo, S. Lee, D. Luong, X. Lin, J. S. R. Vellore Winfred, E. Lochner, I. Fatima, K. Hanson and B. Ma, Efficient Red Light Emitting Diodes Based on a Zero-Dimensional Organic Antimony Halide Hybrid, *Adv. Mater.*, 2022, **34**, e2209417.

47  X. Yang, L.-F. Ma and D. Yan, Facile synthesis of 1D organic–inorganic perovskite micro-belts with high water stability for sensing and photonic applications, *Chem. Sci.*, 2019, **10**, 4567.

48  D. Chen, F. Dai, S. Hao, G. Zhou, Q. Liu, J. Zhao and Z. Xia, Crystal structure and luminescence properties of lead-free metal halides $(C_6H_5CH_2NH_3)_3MBr_6$ (M = Bi and Sb), *J. Mater. Chem. C*, 2020, **8**, 7322–7329.

49  D.-Y. Li, H.-Y. Kang, Y.-H. Liu, J. Zhang, C.-Y. Yue, D. Yan and X.-W. Lei, A 0D hybrid lead-free halide with near-unity photoluminescence quantum yields toward multifunctional optoelectronic applications, *Chem. Sci.*, 2024, **15**, 953–963.

50  M. Cong, B. Yang, F. Hong, T. Zheng, Y. Sang, J. Guo, S. Yang and K. Han, Self-trapped exciton engineering for white-light emission in colloidal lead-free double perovskite nanocrystals, *Sci. Bull.*, 2020, **65**, 1078–1084.

51  T. Chang, H. Wang, Y. Gao, S. Cao, J. Zhao, B. Zou and R. Zeng, Component Engineering to Tailor the Structure and Optical Properties of Sb-Doped Indium-Based Halides, *Inorg. Chem.*, 2022, **61**, 1486–1494.

52  D.-Y. Li, J.-H. Song, Z.-Y. Xu, Y.-J. Gao, X. Yin, Y.-H. Hou, L. J. Feng, C.-Y. Yue, H. Fei and X.-W. Lei, Reversible Triple-Mode Switching in Photoluminescence from 0D Hybrid Antimony Halides, *Chem. Mater.*, 2022, **34**, 6985–6995.

53  Y. Jing, Y. Liu, X. Jiang, M. S. Molokeev, Z. Lin and Z. Xia, $Sb^{3+}$ Dopant and Halogen Substitution Triggered Highly Efficient and Tunable Emission in Lead-Free Metal Halide Single Crystals, *Chem. Mater.*, 2020, **32**, 5327–5334.